Electrochimica Acta 475 (2024) 143582

Contents lists available at ScienceDirect

Electrochimica Acta

journal homepage: www.journals.elsevier.com/electrochimica-acta

About the in-plane distribution of the reaction rate in lithium-ion batteries

Zhenya Wang [a,b], Dmitri L. Danilov [a,c,*], Rüdiger-A. Eichel [a,b], Peter H.L. Notten [a,c,d,*]

[a] Forschungszentrum Jülich (IEK-9), D-52425 Jülich, Germany
[b] Institute of Physical Chemistry, RWTH Aachen University, D-52074 Aachen, Germany
[c] Eindhoven University of Technology, P.O. Box 513, Eindhoven 5600 MB, the Netherlands
[d] University of Technology Sydney, Broadway, Sydney, NSW 2007, Australia

ARTICLE INFO

Keywords:
Reaction rate distribution
Cylindrical batteries
Current density distribution

ABSTRACT

Reaction rate distribution and current density distribution of Li-ion batteries largely determine the local aging and heat generation. Homogenous distribution contributes to better durability and safety of Li-ion batteries. This paper focuses on modeling the in-plane distribution of electrochemical reaction current, and the general equation relating space derivatives of the overvoltage to the electrochemical and electronic current densities is derived. Furthermore, this work investigates the impact of various battery parameters on the distribution by considering the cylindrical battery, one of the most used battery types. An explicit closed-form solution for a short time after the current supplied is obtained. It is found that the dimensions of cylindrical batteries, tabbing design, parameters of current collectors, and electrode materials are all indicated to affect the current density distribution. The electronic current density distribution is also demonstrated. This model and related analyses are incredibly beneficial for further optimizing Li-ion batteries' electronic and electrode properties and as interesting cases for testing battery modeling tools.

1. Introduction

Eco-friendly electric vehicles are considered an effective solution to reduce pollution caused by the excessive use of fossil energy [1,2]. Many countries have issued timetables for discontinuing the sale of conventional fuel vehicles [3,4]. The development of lithium-ion battery technologies is the key factor for electric vehicles [5]. Nevertheless, the inhomogeneous (de)lithiation reaction rate leads to insufficient utilization of electrode material and non-uniform depth of discharge, thus further resulting in localized failure and aging of LIBs [6–8]. Consequently, improving the reaction rate distribution in LIBs is a promising way to reduce energy losses and is increasingly attracting the attention of more researchers worldwide.

Some experiments, such as magnetic field imaging, temperature measurement, or neutron imaging, are reported in the literature to explore the inhomogeneity of the charge-transfer reaction and current density distribution [9–16]. Despite the encouraging results, these experiments are accompanied by certain limitations, notably their demanding nature in terms of time and financial resources. Furthermore, their resolution is still insufficient to determine the reaction rate or current density distribution precisely, especially at short-time scales. As a result, mathematical modeling becomes crucial and advantageous in this context since this approach can evaluate these characteristics precisely over a given time scale and analyze the effects brought by coupling multiple physical and chemical parameters of LIBs [17–23]. This paper proposes a general model that links the reaction rate across the various parts of a battery along with the current collector's position. The derivations are pretty generic, and the universal equation connecting the electrochemical and electronic current densities to the spatial derivatives of the overvoltage is provided. It is possible to study the separate effects on the reaction-rate distribution of the location of tabs, the dimension of the battery, the current collector's resistance, exchange current density, the particle size of the electrode material, and electrode thickness with this model. Moreover, cylindrical lithium-ion batteries are investigated practically as relevant particular cases.

Due to their compact size and high power density, cylindrical lithium-ion batteries are extensively employed as power sources for electric vehicles. They offer several advantages, including easy manufacturing, simple integration with cooling systems, and good mechanical stability [24]. Additionally, cylindrical batteries can withstand high internal and external pressures without causing deformation of the body frame [25]. Furthermore, although larger-format cylindrical

* Corresponding authors at: Forschungszentrum Jülich (IEK-9), D-52425 Jülich, Germany.
E-mail addresses: d.danilov@fz-juelich.de (D.L. Danilov), p.h.l.notten@tue.nl (P.H.L. Notten).

https://doi.org/10.1016/j.electacta.2023.143582
Received 30 August 2023; Received in revised form 1 November 2023; Accepted 26 November 2023
Available online 26 November 2023

batteries like 26,650 or 4680 provide higher energy densities and capacities, the homogeneity of the in-plane distribution of the reaction rate gets worse [2,26–30].

In this work, an explicit analytical solution for the distribution of in-plane electrochemical current density for a short time after applying the current is derived for a cylindrical battery. The effects on the electrochemical current density distribution by tabbing design, parameters of current collectors and electrode materials, and the dimensions of batteries are investigated separately. The variations of electronic current densities along the battery are studied as well. This analysis can be further used to optimize the design of lithium-ion batteries. It can easily be generalized to other types of batteries.

2. Model development

Consider the case of the current density distribution for the unrolled commercial cylindrical Li-ion battery. Fig. 1 shows the schematic diagram of the unrolled 18,650-type cylindrical batteries manufactured by Tianjin Lishen Battery Co. The thicknesses of current collectors are H^* and H_*, respectively. The electrode materials have been coated onto the current collectors. In reality, the width of the tabs is tiny, but they are enlarged in the schematic for better visibility. Between the current collectors is the electrochemical part, including electrodes, electrolyte, separator, etc. The general model for all types of LIBs is developed in the Appendix. Based on Eq. (A36), the following relation holds

$$\frac{\partial^2 J}{\partial x^2}+\frac{\partial^2 J}{\partial y^2}=\frac{\widehat{\rho}^*+\widehat{\rho}_*}{\rho_{bat}}J-\frac{\widehat{\rho}^* I\{(x,y)\in \mathbf{S}^*\}}{\rho_{bat}A^*}-\frac{\widehat{\rho}_* I\{(x,y)\in \mathbf{S}_*\}}{\rho_{bat}A_*}, \tag{1}$$

where

$$\widehat{\rho}^*=\frac{\rho^*}{H^*}, \tag{2}$$

$$\widehat{\rho}_*=\frac{\rho_*}{H_*}, \tag{3}$$

$$\rho_{bat}=\frac{RT}{F}\left(\frac{1}{a_a\delta_a j_a^0}+\frac{1}{a_c\delta_c j_c^0}\right). \tag{4}$$

ρ^*[Ω·m] and ρ_* [Ω·m] are the resistivities of the cathode current collector and anode current collector, respectively. H^* [m] and H_*[m] represent the thickness of the cathode current collector and anode current collector. Additionally, a is the specific interfacial area [m^{-1}], δ is the thickness [m] and j^0 is the exchange current density [A·m^{-2}] of the porous electrode. Subindexes a and c indicate the anodic and cathodic parts. Detailed notations are listed in Table 1.

The unrolled current collector could be regarded as an extended battery strip since the unrolled cylindrical batteries usually have a large aspect ratio. Its width is sufficiently small compared to its length. Suppose the current is uniformly distributed over the tab in the y-direction. Then

$$\frac{\partial J}{\partial y}=0\Rightarrow\frac{\partial^2 J}{\partial y^2}=0. \tag{5}$$

Two specific cases of tab location are considered further, see Fig. 1a and 1b accordingly. According to Eq. (1) for the case I showed in Fig. 1a, when x is in $[0,h]$ one has

$$\frac{d^2 J}{dx^2}=\frac{\widehat{\rho}^* J(x)}{\rho_{bat}}+\frac{\widehat{\rho}_* J(x)}{\rho_{bat}}-\frac{\widehat{\rho}^* I}{\rho_{bat}A}-\frac{\widehat{\rho}_* I}{\rho_{bat}A}. \tag{6}$$

Solving this ordinary differential equation (ODE) produces

$$J=c_1e^{gx}+c_2e^{-gx}+\frac{I}{A}, \tag{7}$$

where

$$g=\sqrt{\frac{\widehat{\rho}^*+\widehat{\rho}_*}{\rho_{bat}}}. \tag{8}$$

Similarly, when x is in $[h,L]$ then

$$\frac{d^2 J(x)}{dx^2}=\frac{\widehat{\rho}^*+\widehat{\rho}_*}{\rho_{bat}}J(x). \tag{9}$$

Solving Eq. (9) yields

$$J=d_1e^{gx}+d_2e^{-gx}. \tag{10}$$

The boundary conditions are as follows (for which more detailed derivations can be found in the supplementary file)

$$\frac{\partial J(0)}{\partial x}=0, \tag{11}$$

$$\frac{\partial J(L)}{\partial x}=0. \tag{12}$$

Applying the boundary conditions results in

$$J=2c\cosh(gx)+\frac{I}{A},\quad 0\le x\le h, \tag{13}$$

and

$$J=2de^{gL}\cosh(g(x-L)),\quad h\le x\le L. \tag{14}$$

Since J is continuous when $x=h$ one can get

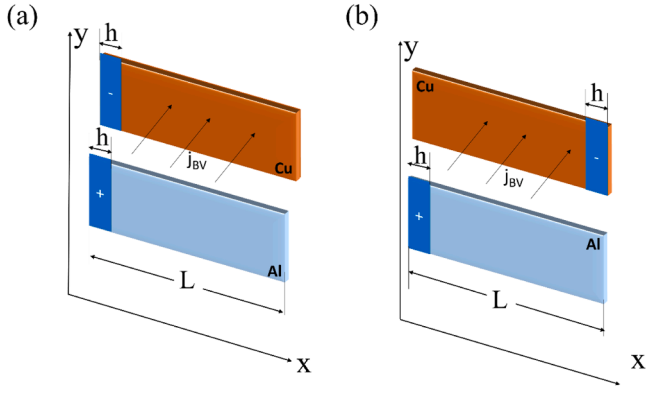

Fig. 1. Layout of the battery when (a) the tabs are on the same side of the battery and (b) tabs are located on both sides of the battery. The thicknesses of current collectors are H* and H*, respectively. Between the current collectors is the electrochemical part, including electrode, electrolyte, separator, etc.

Table 1
Parameter values used in the simulations.

Parameters	Nomenclature	Values	Units
F	Faraday constant	96,485	C•mol^{-1}
h	Width of tabs	3	mm
L	Length	63	cm
W	Width	5.8	cm
H^*	Thickness of cathode CC	10	μm
H_*	Thickness of anode CC	10	μm
A^*	Area of positive tab	$1.7\cdot10^{-4}$	m^2
A_*	Area of negative tab	$1.7\cdot10^{-4}$	m^2
I	Applied current	1	A
a_a	Specific interfacial area of anode	$2.3\cdot10^{5}$	m^{-1}
a_c	Specific interfacial area of cathode	$7\cdot10^{5}$	m^{-1}
ρ_*	Resistivity of anode CC	$1.68\cdot10^{-8}$	Ω·m
ρ^*	Resistivity of cathode CC	$2.28\cdot10^{-8}$	Ω·m
δ_a	Thickness of anode layer	70	μm
j_a^0	Exchange current density of anode	1.6328	A•m^{-2}
δ_c	Thickness of cathode layer	70	μm
j_c^0	Exchange current density of cathode	0.6328	A•m^{-2}

$$J(x)=\begin{cases}2c\cosh(gx)+\dfrac{I}{A}, & 0\le x\le h\\ 2c\cosh(gh)+\dfrac{I}{A}\dfrac{\cosh(g(x-L))}{\cosh(g(L-h))}, & h\le x\le L\end{cases} \tag{15}$$

Moreover, the normalization equation is

$$\int_0^W\int_0^L J(x,y)dxdy=I\Rightarrow\int_0^h J(x)dx+\int_h^L J(x)dx=\frac{I}{W}. \tag{16}$$

Combining Eq. (15) and Eq. (16) results in the final closed-form expression of this case

$$J(x)=\begin{cases}\dfrac{I}{Ae^{gh}}\dfrac{e^{2Lg}-e^{2hg}}{1-e^{2Lg}}\cosh(gx)+\dfrac{I}{A}, & 0\le x\le h\\ \dfrac{I}{Ae^{gh}}\dfrac{e^{2Lg}-e^{2hg}}{1-e^{2Lg}}\cosh(gh)+\dfrac{I}{A}\dfrac{\cosh(g(x-L))}{\cosh(g(L-h))}, & h\le x\le L\end{cases} \tag{17}$$

Case II, shown in Fig. 1b, is investigated subsequently. Positive and negative tabs are placed symmetrically around the central point of the battery band. For modeling convenience, the origin of the coordinate system is moved to the midpoint of the battery.

The equation over the entire interval can be written as

$$\frac{d^2J}{dx^2}=\frac{\widehat{\rho}^*+\widehat{\rho}_*}{\rho_{bat}}J(x)+\begin{cases}-\dfrac{I}{\rho_{bat}A}\left(\dfrac{\widehat{\rho}^*+\widehat{\rho}_*}{2}+\dfrac{\widehat{\rho}^*-\widehat{\rho}_*}{2}\right), & -\dfrac{L}{2}\le x\le-\dfrac{L}{2}+h\\ 0, & -\dfrac{L}{2}+h\le x\le\dfrac{L}{2}-h\\ -\dfrac{I}{\rho_{bat}A}\left(\dfrac{\widehat{\rho}^*+\widehat{\rho}_*}{2}-\dfrac{\widehat{\rho}^*-\widehat{\rho}_*}{2}\right), & \dfrac{L}{2}-h\le x\le\dfrac{L}{2}\end{cases}. \tag{18}$$

Consider the total solution as a sum of symmetric and antisymmetric parts as

$$J(x)=J_s(x)+J_a(x). \tag{19}$$

Applying notation Eq. (8) to the symmetric part gives

$$\frac{d^2J_s}{dx^2}=g^2J_s(x)+\begin{cases}-\dfrac{I}{2A}g^2, & -\dfrac{L}{2}\le x\le-\dfrac{L}{2}+h\\ 0, & -\dfrac{L}{2}+h\le x\le\dfrac{L}{2}-h\\ -\dfrac{I}{2A}g^2, & \dfrac{L}{2}-h\le x\le\dfrac{L}{2}\end{cases}. \tag{20}$$

Note that Eq. (20) corresponds to the physical case when the positive and negative sides of the current collector have the same resistance. In this case, normal boundary conditions on both left and right edges apply, i.e. $\frac{\partial J_s(-L/2)}{\partial x}=\frac{\partial J_s(L/2)}{\partial x}=0$. Only half of the solution is considered due to symmetry. That yields

$$\frac{d^2J_s}{dx^2}=g^2J_s(x)+\begin{cases}0, & 0\le x\le\dfrac{L}{2}-h\\ -\dfrac{I}{2A}g^2, & \dfrac{L}{2}-h\le x\le\dfrac{L}{2}\end{cases}. \tag{21}$$

The boundary equations are

$$\frac{\partial J_s(0)}{\partial x}=\frac{\partial J_s(L/2)}{\partial x}=0. \tag{22}$$

Combine Eq. (22), the continuity equation, and the normalization equation to get the analytical solution of J_s (see detailed derivations in the supplementary information).

$$J_s(x)=\begin{cases}2c\cosh(gx), & 0\le x\le\dfrac{L}{2}-h\\ 2c\cosh\left(g\left(\dfrac{L}{2}-h\right)\right)-\dfrac{I}{2A}\dfrac{\cosh\left(g\left(x-\dfrac{L}{2}\right)\right)}{\cosh(gh)}+\dfrac{I}{2A}, & \dfrac{L}{2}-h\le x\le\dfrac{L}{2}\end{cases}, \tag{23}$$

where $c=\frac{I}{4A}\frac{\sinh(gh)}{\sinh(gL/2)}$.

Then, for the asymmetric part

$$\frac{d^2J_a}{dx^2}=g^2J_a(x)+\begin{cases}-\dfrac{I}{\rho_{bat}A}\dfrac{\widehat{\rho}^*-\widehat{\rho}_*}{2}, & -\dfrac{L}{2}\le x\le-\dfrac{L}{2}+h\\ 0, & -\dfrac{L}{2}+h\le x\le\dfrac{L}{2}-h\\ \dfrac{I}{\rho_{bat}A}\dfrac{\widehat{\rho}^*-\widehat{\rho}_*}{2}, & \dfrac{L}{2}-h\le x\le\dfrac{L}{2}\end{cases}. \tag{24}$$

Similar to Eq. (8), introduce notation

$$k^2=\frac{\widehat{\rho}^*-\widehat{\rho}_*}{\rho_{bat}}. \tag{25}$$

Then, substitute Eq. (25) into Eq. (24) to obtain

$$\frac{d^2J_a}{dx^2}=g^2J_a(x)+\begin{cases}-\dfrac{I}{2A}k^2, & -\dfrac{L}{2}\le x\le-\dfrac{L}{2}+h\\ 0, & -\dfrac{L}{2}+h\le x\le\dfrac{L}{2}-h\\ \dfrac{I}{2A}k^2, & \dfrac{L}{2}-h\le x\le\dfrac{L}{2}\end{cases}. \tag{26}$$

The boundary conditions are

$$J_a(0)=\frac{\partial J_a(L/2)}{\partial x}=0. \tag{27}$$

Finally, the closed-form solution is

$$J_a(x)=\begin{cases}2c\sinh(gx), & 0\le x\le\dfrac{L}{2}-h,\\ 2c\sinh\left(g\left(\dfrac{L}{2}-h\right)\right)+\dfrac{I}{2A}\dfrac{k^2}{g^2}\dfrac{\cosh\left(g\left(x-\dfrac{L}{2}\right)\right)}{\cosh(gh)}-\dfrac{I}{2A}\dfrac{k^2}{g^2}, & \dfrac{L}{2}-h\le x\le\dfrac{L}{2},\end{cases} \tag{28}$$

where $c=-\frac{I}{A}\frac{\frac{k^2}{g^2}\sinh(gh)}{4\cosh\left(\frac{gL}{2}\right)}$, for which detailed derivations are from the supplementary file. The final $J(x)$ is the sum of $J_a(x)$ and $J_s(x)$ according to Eq. (19).

Moreover, the electronic current density distribution along the position of current collectors is also studied. It can be obtained by the conservation law, and the expression is

$$\mathrm{div}(J_e)=J+\frac{I\{(x,y)\in\mathbf{S}_*\cup\mathbf{S}^*\}}{A}, \tag{29}$$

where A represents the area of the union of $\mathbf{S}^*$ and $\mathbf{S}_*$. Solving Eq. (29) yields the closed-form solution of the electronic current density J_e, which is orthogonal to J. The detailed derivations and final results for cases I and II can be found in the supplementary information.

3. Results and discussion

The derivation of Eq. (A18) is completely universal and can be used for all types of batteries. This general equation establishes the relationship between the space derivatives of the overvoltage, the electrochemical current density, and the input/output current densities. Parameters like the applied current and current densities can be time-dependent, which allows for calculating the instantaneous change of

the battery over time. In that case, suitable finite-difference methods must be applied. The most straightforward assumption will be to presume negligible ionic flux across the in-plane direction. That is logical because electronic conductivity in metals usually is many orders of magnitude larger than the ionic conductivity of a typical battery electrolyte. The same can be said about electronic flux inside active electrode materials. Then the relation between battery overvoltage $\eta(x,y)$ and local electrochemical current density $J(x,y)$ can be simulated by any pseudo-two-dimensional model, including Neumann-type [19,31–34] or Nernst-Planck-type [35–38] applied (x, y)-pointwise. After applying boundary and normalization conditions that will produce $J(x,y)$ satisfying Eq. (A18), which is in agreement with the employed battery model. However, such an approach requires heavy numerics and, though absolutely general, lacks transparency and intuition.

Using linearized Butler–Volmer relation and relatively mild assumption, Eq. (A26) and Eq. (A29) are derived. They are much simpler and can be studied qualitatively and quantitatively. It could be concluded that the electrochemical current density on the entrance to the electrode and the reaction rate on the walls of the pores are proportional to each other. All electrons passing from the current collector to the electrode material will be spent on the walls of the pores during the charge transfer reaction.

The current collectors are often regarded as infinitely conductive or counted in total ohmic resistance in most existing lithium-ion battery models [1,37–39]. In contrast, the model introduced in the previous section emphasizes the role of current collectors. In particular, current collectors' resistivity and thickness affect the potential and current density distribution, as expressed in Eq. (A34) and Eq. (A35). These equations imply that the sheet resistance of current collectors definitely influences the (in-)homogeneity of the current density.

Another critical parameter defined by Eq. (A33) could be the total Bulter–Volmer resistance. The combination of it and the sheet resistance of current collectors finally determines the electrochemical current density distribution. As shown in Eq. (A36), the equation depends on all design parameters only through combinations $\frac{\widetilde{\rho}^*}{\rho_{bat}}$ and $\frac{\widehat{\rho}_*}{\rho_{bat}}$. For example, the solution will not change if the sheet resistance and the total Bulter–Volmer resistance are increased twice. Besides, the terms $\frac{I\{(x,y)\in \mathbf{S}^*\}}{A^*}$

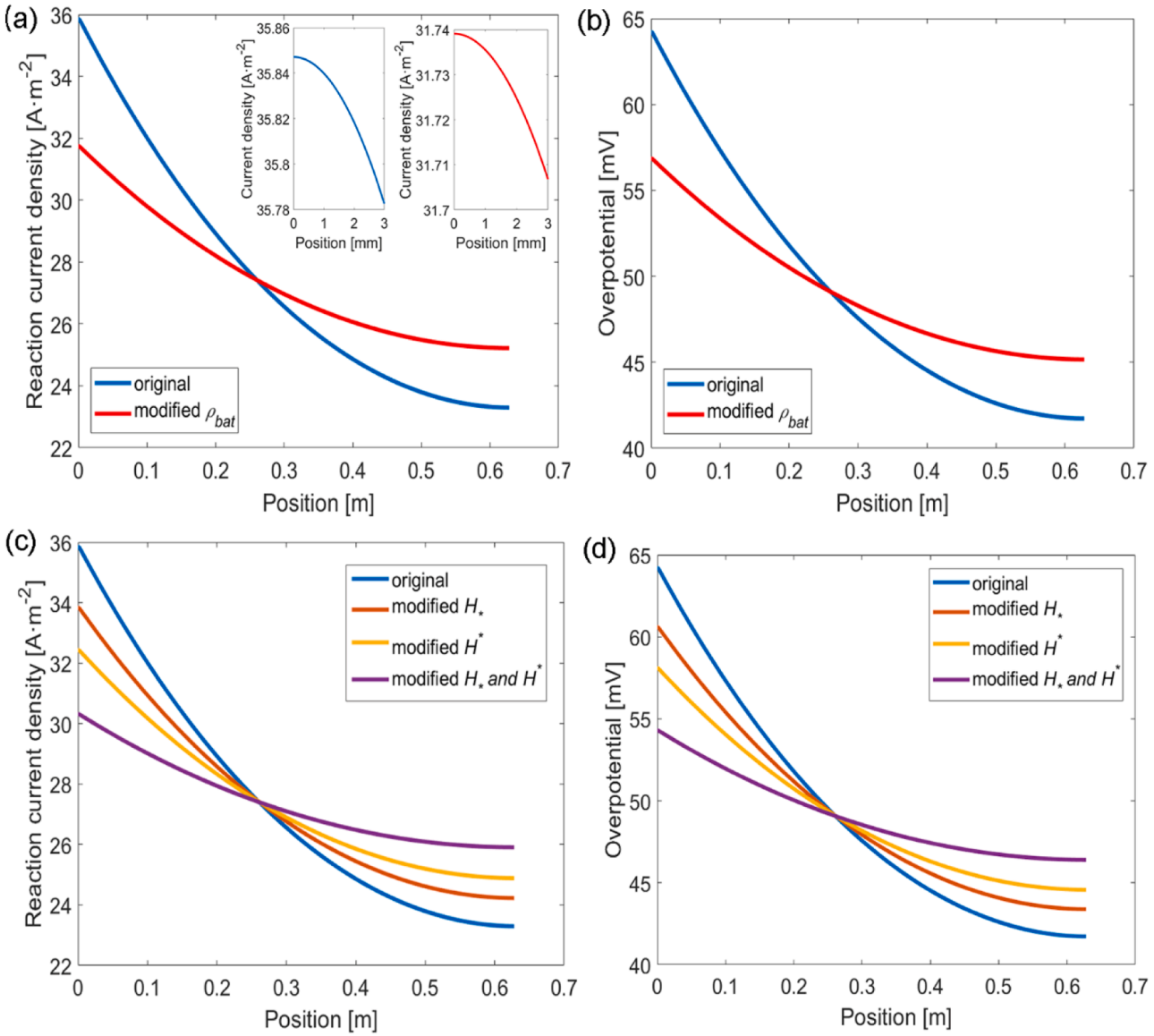

Fig. 2. (a) Current density distribution for case I. Inset is the enlarged distribution parts along the tab; (b) Overpotential distribution for case I. The two curves are related to the parameters of the original cell parameters and the modified parameters, respectively; (c) Current density distribution and (d) Overpotential distribution for the original parameters and modified H^*, H_*.

and $\frac{I\{(x,y)\in \mathbf{S}_*\}}{A_*}$ in Eq. (A36) are essentially current densities as well, which means every term is about current density. That stresses the consistency and coherence of this model.

Subsequently, the current density distribution and overpotential distribution of case I for cylindrical batteries are plotted in Fig. 2. The blue line shows the results with the original battery parameters. The inset parts are the enlarged areas of the tabs. As shown in Fig. 2a, the electrochemical current density is highest at the tabs. Then, it decreases along the length of the current collector, which is also consistent with the reports from previous literature [13,40–42]. That is because all current passes via the tabs into the current collector and finally goes into the electrode. This area is also where the most heat is produced. The larger the distance from the tab, the more severe the current density decays. The material utilization at more distant locations will be significantly lower than near the tabs. The trend of the reaction rate is the same as the current density according to derivation Eq. (A26). That suggests the reaction rate near the tab region is also much higher. Fig. 2b shows the overpotential distribution that caused the inhomogeneous current density [43]. The polarization at tabs is about 65 mV, while it drops to about 43 mV at the farthest distance from tabs. Since Eq. (1) implies that ρ_{bat} has a significant impact on the current density distribution, the sensitivity analysis of the distribution with respect to $\rho_{bat}$is studied. Modified ρ_{bat} contributes to more homogenous current density and reaction rate distribution, as illustrated by the red curve in Fig. 2. Specifically speaking, the inhomogeneity is calculated as $\frac{J_{\max}-J_{\min}}{J_{\max}} \times 100\%$. It is decreased from 36 % to 19 % when ρ_{bat} becomes 2 times larger. That means the parameters, including the specific interfacial area of the electrode, electrode thickness, and the exchange current density are essential for improving the current density distribution. The impacts of these parameters are discussed separately in more detail further.

More importantly, it could be inferred from the final solution that the combination of parameters g (given by Eq. (8)) plays a crucial role in the electrochemical current density distribution. Most battery parameters enter into the solution only as the function of g, which emphasizes the importance of the ratio between ρ_{bat}, $\widehat{\rho}^*$and $\widehat{\rho}_*$. Therefore, the sheet resistance of current collectors is also supposed to affect the current density distribution. The thickness of the current collectors is highly related to the sheet resistance [44–47], and thicker current collectors lead to smaller resistance. Fig. 2c and d demonstrate the influence of various thicknesses of the current collectors on the current density and overpotential distribution. In total, three combinations of parameters are explored. That includes increasing the thickness of the positive current collector by 15 μm, then doing the same with the negative current collector, and finally increasing the thickness of both current collectors simultaneously.

The blue line corresponds to the original set of parameters. In contrast, the yellow line indicates the case when the cathode current collector is increased to 25 μm. It can be concluded that smaller resistance led by the thicker current collector results in a more homogeneous reaction rate distribution and better utilization of the electrode materials. It is worth noting that increasing the thickness to the same extent on the positive and negative current collectors brings different effects. The benefits of modifying the positive current collector will be explicitly studied further. The conductivity of aluminum, generally used for the positive current collector, is worse than the copper used for the opposing side [48]. The improvement should concentrate on the weak point, and addressing worse shortcomings leads to better results.

Consequently, despite increasing the same thickness, the improvement on the positive side will be more pronounced. Enhancing the conductivity of the aluminum current collector is more economical and more effective. In addition, it can be observed from Fig. 2c and d that the inhomogeneity of the electrochemical current density and overpotential is improved more noticeably if the resistance of both positive and negative current collectors is simultaneously modified. However, the reader should be aware that the possibility of increasing the thickness of current collectors is limited. Although thicker current collectors result in lower resistance, the cost of the battery increases, and the energy density declines. The overall battery performance and costs should be optimized simultaneously when designing the current collectors.

Fig. 3a illustrates the current density distribution in different cases. The current density looks convex and highest at the tabs on both sides in case II. It can be concluded that the current density and reaction rate distribution are much more homogenous when the tabs are placed at both ends of the battery compared to case I. The inhomogeneity of case II is reduced from 36 % to 16 %. That should also decrease the localized temperature and the possibility of internal short circuits [48,49]. Therefore, this study supports the idea that reasonable tab positions contribute to less heat generated and improve safety and reliability.

Additionally, placing the tabs on different sides could prevent manufacturing process defects coming from overlapping tabs [50,51]. It can be inferred that adding more tabs might bring more homogenous current distribution and reduce the temperature gradient inside the battery. However, too many tabs also significantly increase the cost of the batteries. Fig. 3b shows the overpotential of two cases that also strongly depend on the position. Similarly, the overpotential of case II is smaller than case I, which means optimizing the position of the tabs leads to smaller polarization and power losses.

On the other hand, it is interesting that case II demonstrates the reaction current density on the positive side is greater than on the negative side because the resistance of the aluminum foil is greater than that of the copper foil at the same thickness. The resistance of the current collector can be changed by using different materials or changing the thickness. Fig. 3c and d illustrates the current density and overpotential distribution after optimizing the thickness of current collectors. The distribution becomes more uniform in both cases, which suggests this method is effective regardless of the tab location. The inhomogeneity of case I is reduced to 17 % from 36 % while in case II it is goes down to 5 % from 16 %. The thickness of the current collector must be increased appropriately to bring such a substantial improvement. It is worth emphasizing that the thicknesses of current collectors on both sides of case II here are optimized to make their resistances equal. The thickness of cathode current collectors is simply increased by 6 μm. This situation is the most suitable since the asymmetric part in Eq. (24) disappears. As shown in Fig. 3c and d, the current density and overvoltage at the left and right ends of the red lines are identical in this case, which implies the best scenario with the most homogeneous reaction rate distribution.

The 3D plot of Fig. 4a further investigates the effects of the thickness of the aluminum current collector on the current density distribution. As the thickness of the aluminum foil increases, its resistance continues to become smaller, and it can be seen that the current density distribution becomes more homogeneous. That is essentially what Eqs. (18) and (25) indicate. According to Eq. (19) $J(x)$ consists of symmetric and asymmetric parts, and the asymmetric part determines the difference in current density between the two sides. As the difference in the resistance of the positive and negative current collectors decreases, the asymmetric part becomes less visible. If they have the same sheet resistance, then the current density will be symmetrically distributed along the midline of the battery, which also can be observed in Fig. 4a. Coupled with the results of case I, it can be concluded that optimizing the thickness of the current collectors is a prospective way to improve the reaction rate distribution and material utilization. Increasing the thickness by a few microns can bring significant enhancements. This conclusion is also consistent with the discussion about Fig. 3c and d above. This method might be more efficient and affordable. It is less complex than adding or shifting tabs.

The effects of other battery parameters on the electrochemical current density distribution are further studied. Fig. 4b indicates that decreasing the specific area of the electrode materials can improve the homogeneity of the current density distribution. Changing the active material's particle size and volume fraction will impact the specific interfacial area. Reducing the particle size of the electrode material

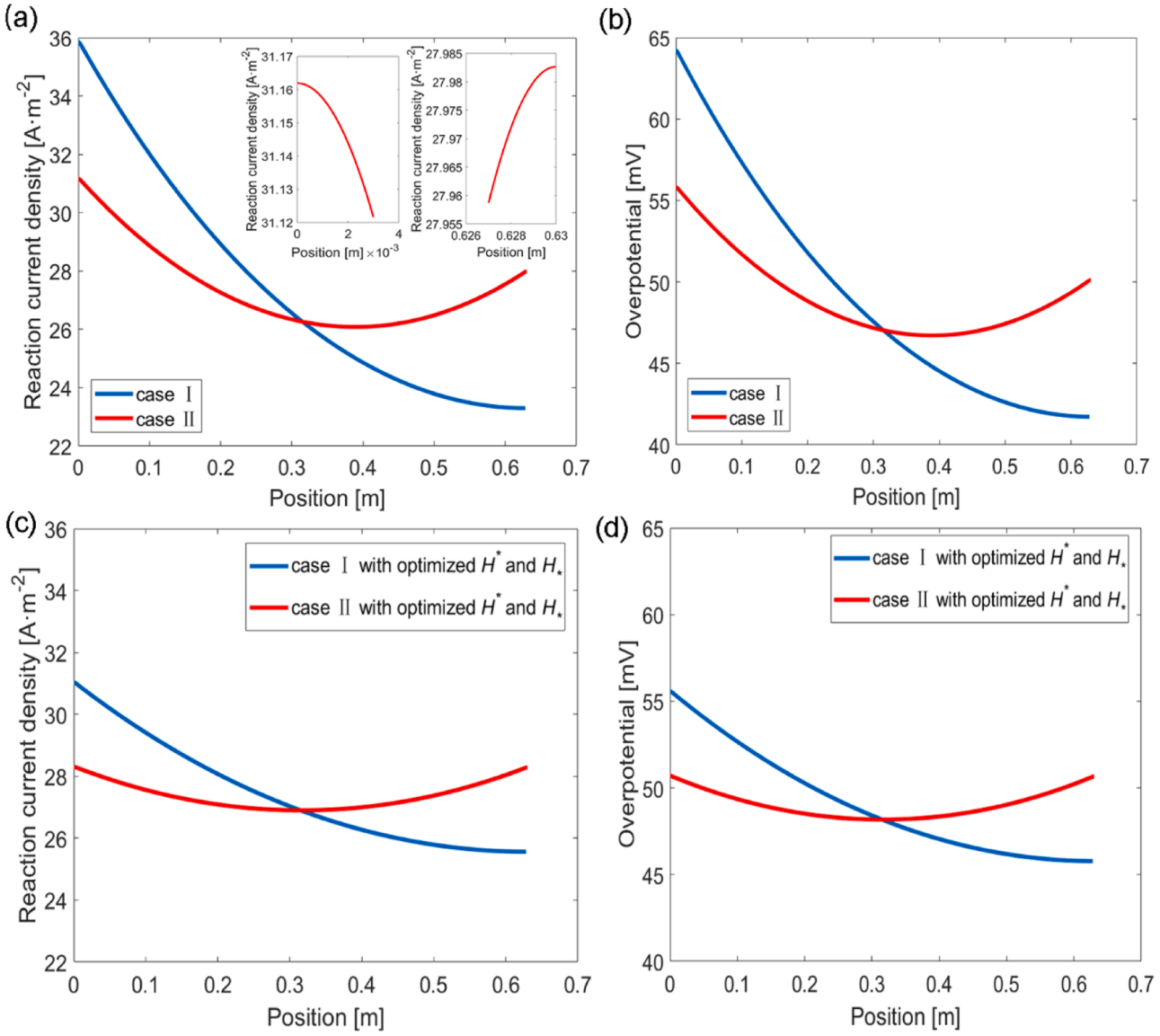

Fig. 3. (a) Current density distribution and (b) overpotential distribution for case I and case II. Insets are the enlarged distribution parts along the tabs. (c) Current density distribution and (d) overpotential distribution with optimized CC thickness.

usually leads to a larger specific surface area and, thus, to a higher power density [52–54]. Nevertheless, it can be deferred from Fig. 4b that improvements in electrode material kinetics must be accompanied by enhancements in the electronic part since additional limitations exist on the battery level. Assuming that the parameters of the current collectors are kept constant and only improvements are made to the material level, then at some moment, the inhomogeneity of electrochemical current density and material utilization comes into play, which is detrimental to the overall performance of the battery.

In addition, increasing the thickness of the battery electrodes can usually be used to maximize energy density or capacity. However, excessive thickness affects the material utilization. Fig. 4c and d also prove this point. It can be observed that as the electrode thickness increases, the electrochemical current density becomes more inhomogeneous. Correspondingly, the difference in reaction rate along the various positions of the battery turns out to be more significant. That is because the over-thickness of the electrode leads to smallerρ_{bat}, further implying that more lithium ions are inclined to be consumed near tabs. Consequently, finding optimally thick electrodes is the best way to improve the performance of batteries [55,56]. Moreover, as shown in Fig. 4d, the effect of changing the thickness of the anode is more obvious in this case, which may be due to the different properties of the cathode and anode materials.

According to the parameterρ_{bat}, the current distribution is also influenced by the exchange current density. Although an increase in the exchange current density implies better surface kinetics, as shown in Fig. 4e, high exchange current density can also affect the overpotential and thus result in increasing the disparity in current density between various positions. Based on the modeling results, there is a saturation value of the exchange current density, beyond which its effect on the reaction rate hardly changes. This saturation value is different for the cathode and anode.

On the other hand, widening the tabs is beneficial for the homogeneous reaction rate distribution. As illustrated in Fig. 4f, wider tabs allow for more uniform current entry [11], leading to a smaller difference between the current density at the tabs and elsewhere. The current density decay along the width of the tabs is also smoother. Not surprisingly, increasing the widths of tabs helps decrease the maximum temperature greatly and further reduces the safety hazards [49]. Besides, the aspect ratio of the battery affects the current density

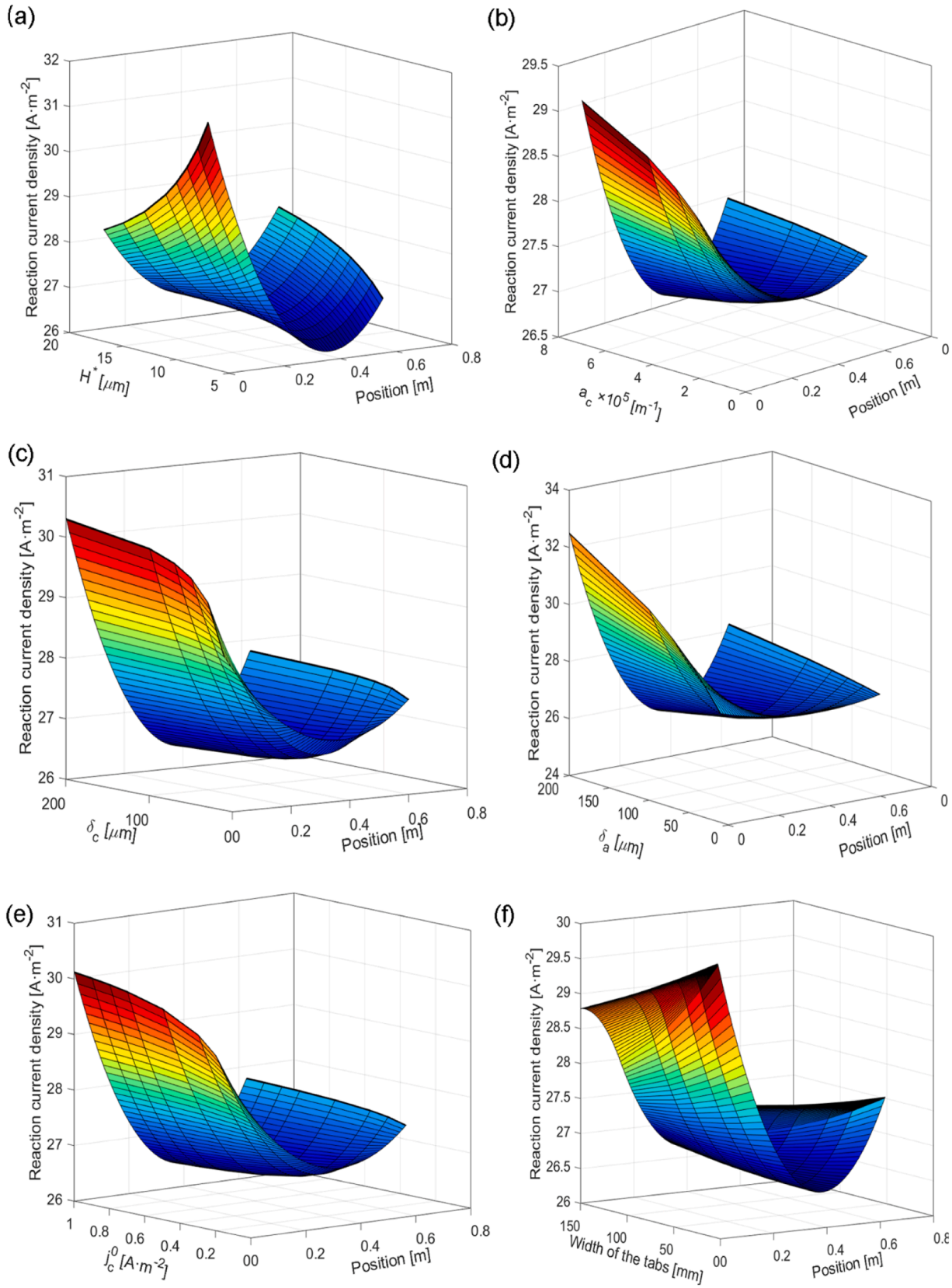

Fig. 4. The effects of (a) the thickness of the current collector on cathode side; (b) specific area of cathode; (c) thickness of cathode; (d) thickness of anode (e) exchange current density of cathode; (f) width of the tabs on the electrochemical current density distribution.

distribution. Fig. 5a and b demonstrate the distribution of electrochemical current density when the lengths are increased to 2 times and 4 times the original lengths, respectively. The embedded graph is the distribution with the original length for comparison. It can be concluded that longer electrodes will cause the current not to reach the positions far away from the tab. With the increasing length of the electrodes, the current density and reaction rate in some places approaches 0, which results in the severely inhomogeneous utilization of materials and local aging of batteries. Optimizing the sheet resistance of the current collector as much as possible in this case can still lead to some improvement in the inhomogeneity, as indicated in Fig. 5a and b. Additionally, the 3D plot of current density distribution under different lengths for case II is illustrated in Fig. 5c. The position is normalized, and the current density decreases as the length increases. As a result, the distribution of current density and reaction rate becomes increasingly inhomogeneous as the aspect ratio rises. This point should be kept in mind when developing large-format batteries. The modeling results also show that case II still has a better current density distribution with an optimized thickness.

The electronic current density of case I is illustrated in Fig. 6a, in which the blue curve represents the tabs part. It can be seen that the electronic current varies tremendously at tabs and then becomes zero at the opposite end of the band. That means that electrons are entering the current collectors in the tab area. The current at tabs is the highest; thus, more charge transfer is happening there. Fig. 6b shows the electronic current distribution in case II. When the tab is located on both sides of the battery, the electronic current densities are also mirrored images of each other. Similarly, the electronic current is highest and consumed faster at tabs and becomes zero at one end of the battery. Besides, Fig. 6c–f demonstrate the distribution of electronic current density when the lengths of batteries become 2 and 4 times longer. It could be observed that the electronic current density changes quickly at the tabs while being smooth at other positions. The nonlinearity in Fig. 6f may be attributed to the interplay between the anode and cathode sides. They affect each other while contributing to the resistance.

4. Conclusion

The in-plane electrochemical current density distribution and reaction rate distribution are derived for a short moment after applying the current. The link between the current densities and the spatial

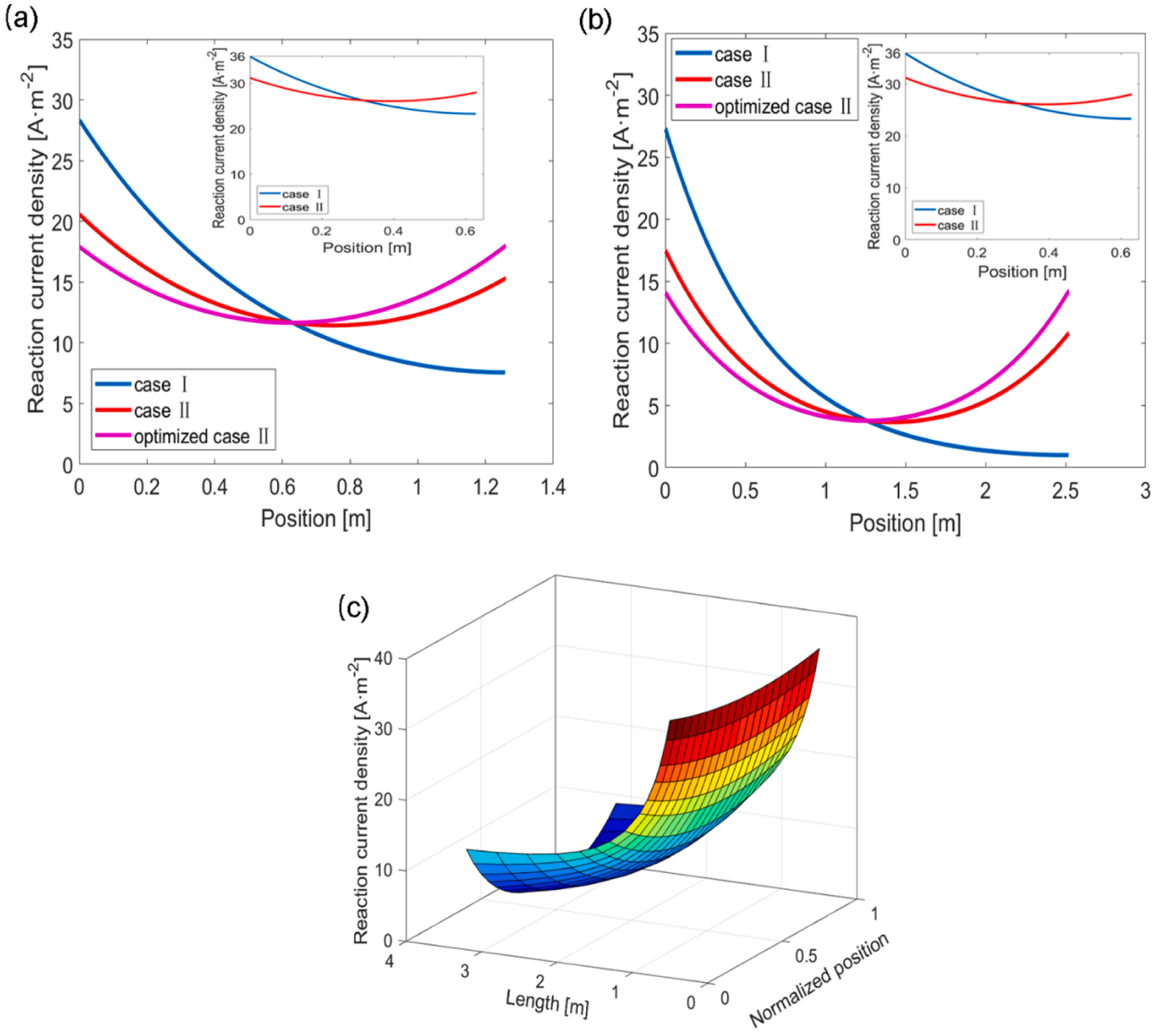

Fig. 5. Distribution of electrochemical current density along the current collector when the length is enlarged 2 times (a) and 4 times (b), respectively. The inset plot is the distribution with the original length provided for comparison. (c) 3D plot for the current density distribution under different lengths for case II.

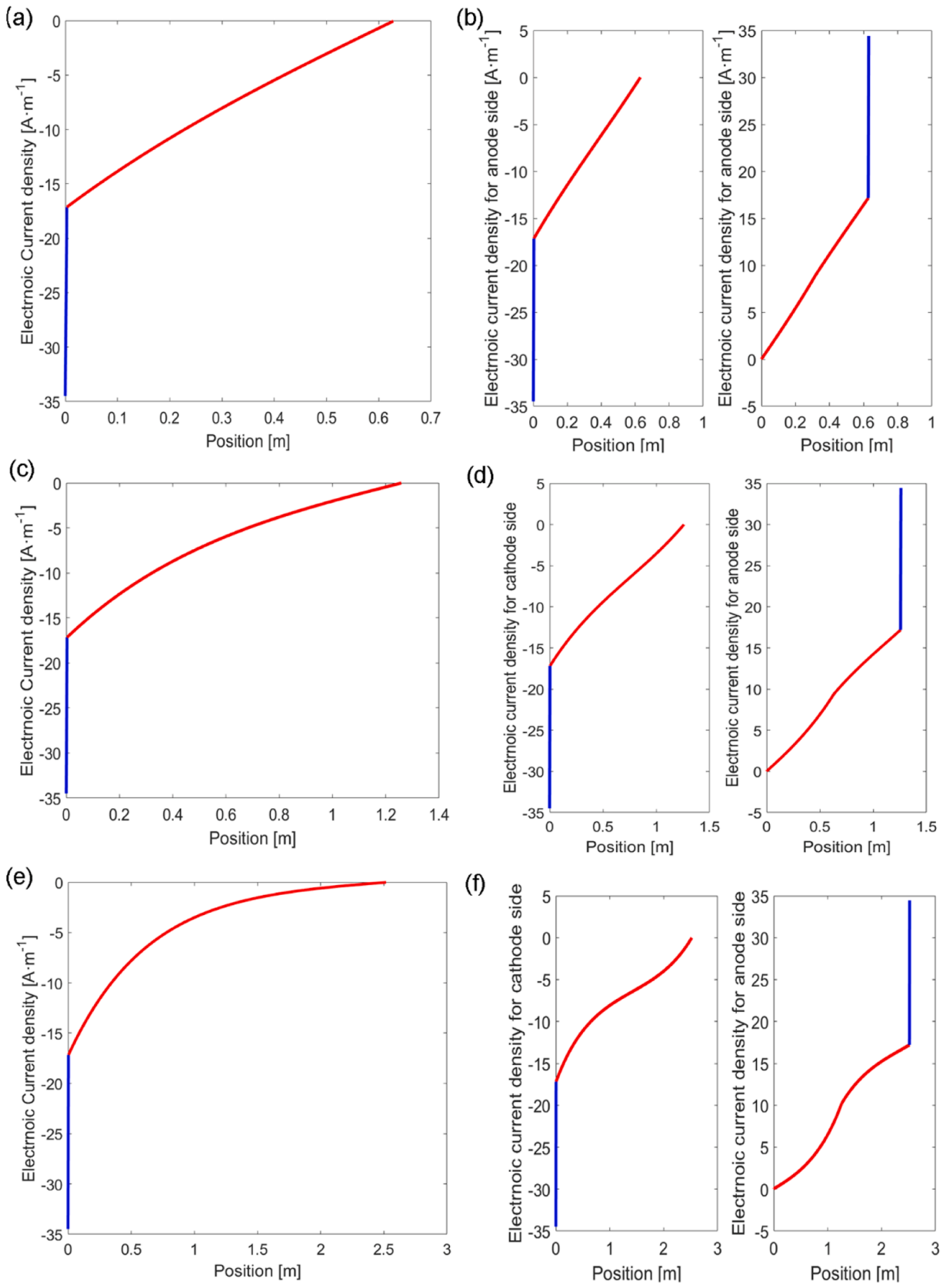

Fig. 6. The electronic current density distribution of case I (a), (c), (e); and case II (b), (d), (f) under different lengths.

derivatives of the overvoltage is clarified. The analytical solution of cylindrical lithium-ion batteries' current density distribution is obtained. It is found that optimizing the tabbing design and the resistance of current collectors significantly improves the current density and reaction rate distribution of cylindrical batteries. Moreover, some battery parameters, such as a smaller aspect ratio of batteries and electrode thickness, also contribute to a more homogenous (de)lithiation reaction rate distribution and thus reduce the risk of local aging and thermal runaway. This work highlights interesting design suggestions that can enhance cylindrical batteries' overall performance. The effects of the electronic and electrode components should be fully considered when designing the batteries. Similar derivations can be straightforwardly performed for other types of batteries.

CRediT authorship contribution statement

Zhenya Wang: Investigation, Software, Validation, Data curation, Writing – original draft. **Dmitri L. Danilov:** Conceptualization, Methodology, Software, Supervision, Writing – review & editing. **Rüdiger-A. Eichel:** Project administration. **Peter H.L. Notten:** Conceptualization, Supervision, Writing – review & editing.

Declaration of Competing Interest

The authors declare that they have no known competing financial interests or personal relationships that could have appeared to influence the work reported in this paper.

Data availability

Data will be made available on request.

Acknowledgments

The author Z. Wang gratefully acknowledges fellowship support by the China Scholarship Council. Dr. D.L. appreciates the support from the grant ProMoBiS (grant Number. 03ETE046C, BMBF, Germany).

Supplementary materials

Supplementary material associated with this article can be found, in the online version, at doi:10.1016/j.electacta.2023.143582.

Appendix

Consider the layout of the (rechargeable) battery illustrated in Fig. A1. Batteries consist of a cathode current collector, cathode material, separator area, anode material, and anode current collector. As a first approximation, one can assume flat geometry with constant thicknesses of all parts. As denoted in Fig. A1, the current collector material for the cathode side is usually aluminum, and copper for the anode side. The middle part between the two current collectors is related to electrochemistry. The current collector has the dimensions of length (L), width (W), and thickness (H^*), as shown in Fig. A1. The areas of the blue rectangle represent the positions of the input currents, namely the battery's cathode tab. The surface area in the cathode where the tab touches the current collector will be denoted by $\mathbf{S}^*$. Geometrically, $\mathbf{S}^*$ lies in xy plane, where $z = 0$. The corresponding area on the anode is denoted by $\widetilde{S}_*$, and its projection to xy plane as $\mathbf{S}_*$. The direction of the current during charging out of $\widetilde{S}_*$ area, as the blue arrow demonstrates. The following notations introduced in [44] lead to

$$\Delta\varphi^* + \frac{1}{H^*}\left[\frac{\partial\widetilde{\varphi}(x,y,H^*)}{\partial z} - \frac{\partial\widetilde{\varphi}(x,y,0)}{\partial z}\right] = 0, \tag{A1}$$

where $\widetilde{\varphi}$ [V] is the galvanic potential function considered as a function of three space variables, i.e. (x,y,z), the average of the 3D potential $\widetilde{\varphi}$ with respect to the thickness. Eq. (A1) can be rewritten as

$$\Delta\varphi^* = S^* + D^*. \tag{A2}$$

where

$$S^* = S^*(x,y) = \frac{1}{H^*}\frac{\partial\widetilde{\varphi}(x,y,0)}{\partial z}, \tag{A3}$$

and

$$D^* = D^*(x,y) = -\frac{1}{H^*}\frac{\partial\widetilde{\varphi}(x,y,H^*)}{\partial z}. \tag{A4}$$

Assume that current I [A] is supplied to the current collector via the area $\mathbf{S}^*$with a surface area A^* [m^2]. The input current is assumed to be uniformly distributed across all points of $\mathbf{S}^*$. A combination of Eqs. (A3) and (A4) with the differential form of Ohm's law, gives

$$S^* = -\frac{\rho^* I\{(x,y) \in \mathbf{S}^*\}}{H^* A^*}, \tag{A5}$$

and

$$D^* = \frac{\rho^* J(x,y)}{H^*}, \tag{A6}$$

where S^* represents the term responsible for the current supplied to the cathode through the area current collector, and ρ^* [Ω·m] is the resistivity of the cathode current collector.

In contrast, D^* is related to the electrochemical current on the surface area of the cathode current collector. $J(x,y)$ [A·m^{-2}] represents the electronic current density passing across the interface between the current collector and the active electrode material. Similarly, for the anode current collector, one can get

$$\Delta\varphi_* = -\frac{1}{H_*}\left[\frac{\partial\widetilde{\varphi}_*(x,y,z_{out})}{\partial z} - \frac{\partial\widetilde{\varphi}_*(x,y,z_{in})}{\partial z}\right] = S_* + D_*, \tag{A7}$$

where

$$S_* = -\frac{1}{H_*}\frac{\partial\widetilde{\varphi}_*(x,y,z_{out})}{\partial z} = \frac{\rho_* I\{(x,y)\in \mathbf{S}_*\}}{H_* A_*}, \tag{A8}$$

$$D_* = \frac{1}{H_*}\frac{\partial\widetilde{\varphi}_*(x,y,z_{in})}{\partial z} = -\frac{\rho_* J(x,y)}{H_*}, \tag{A9}$$

where z_{in} and z_{out} represent z coordinates of the inner and outer sides of the anode current collector, respectively. ρ_* [Ω·m] is the resistivity of the anode current collector, and H_* [m] is the thickness of the anode current collector.

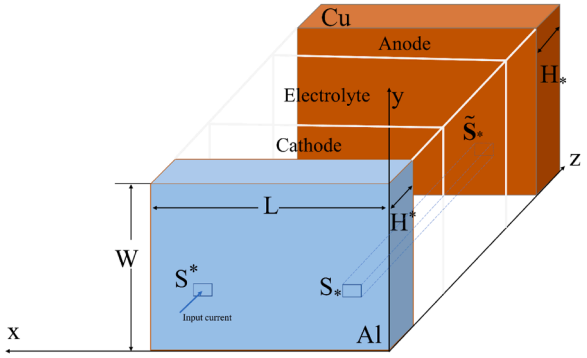

Fig. A1. Layout of the lithium-ion battery.

The voltage over the battery can be written as

$$V = \varphi^* - \varphi_*. \tag{A10}$$

Differentiating Eq. (A10) yields

$$\frac{\partial V}{\partial x} = \frac{\partial\varphi^*}{\partial x} - \frac{\partial\varphi_*}{\partial x}, \tag{A11}$$

$$\frac{\partial V}{\partial y} = \frac{\partial\varphi^*}{\partial y} - \frac{\partial\varphi_*}{\partial y}. \tag{A12}$$

Eqs. (A11) and (A12) also can be derived from Kirchhoff's voltage law, for which more detailed derivations can be found in the supplementary file. Find the second-order partial derivative of Eqs. (A11) and (A12)

$$\frac{\partial^2 V}{\partial x^2} = \frac{\partial^2\varphi^*}{\partial x^2} - \frac{\partial^2\varphi_*}{\partial x^2}, \tag{A13}$$

$$\frac{\partial^2 V}{\partial y^2} = \frac{\partial^2\varphi^*}{\partial y^2} - \frac{\partial^2\varphi_*}{\partial y^2}. \tag{A14}$$

Subtracting Eq. (A14) from Eq. (A13) brings

$$\Delta V = \Delta\varphi^* - \Delta\varphi_* = S^* + D^* - D_* - S_*. \tag{A15}$$

Combination of Eq. (A15) with Eq. (A5), (A6), (A8), and (A9) gives

$$\Delta V = -\frac{\rho^* I\{(x,y)\in \mathbf{S}^*\}}{H^* A^*} + \frac{\rho^* J(x,y)}{H^*} - \frac{\rho_* I\{(x,y)\in \mathbf{S}_*\}}{H_* A_*} + \frac{\rho_* J(x,y)}{H_*}. \tag{A16}$$

Since battery voltage is a summation of equilibrium battery voltage and overpotential, it follows that

$$\Delta V = \Delta(E+\eta), \tag{A17}$$

where η represents the overpotential and E is the equilibrium potential. Then

$$\Delta\eta = \Delta V - \Delta E = -\frac{\rho^* I\{(x,y)\in \mathbf{S}^*\}}{H^* A^*} + \frac{\rho^* J(x,y)}{H^*} - \frac{\rho_* I\{(x,y)\in \mathbf{S}_*\}}{H_* A_*} + \frac{\rho_* J(x,y)}{H_*} - \Delta E. \tag{A18}$$

Assume that the battery remains in equilibrium until the current is switched on. Then, there is no difference between various points in the current collector and $\Delta E = 0$. Suppose that the applied current produces a sufficiently small overvoltage so that the Butler-Volmer equation is simplified to the

linear relationship by

$$j_{BV} = \frac{j^0}{F}\left[e^{\frac{\alpha F\eta}{RT}} - e^{-\frac{(1-\alpha)F\eta}{RT}}\right] \approx \frac{j^0\eta}{RT} \quad \text{or } \eta = \frac{RT}{j^0}j_{BV}, \tag{A19}$$

where j_{BV} denotes the reaction rate [mol·m^{-2}·s^{-1}], j^0 the exchange current density [A·m^{-2}], F the Faraday constant [C·mol^{-1}], R the universal gas constant [J·mol^{-1} K^{-1}] and T the absolute temperature [K]. Note that j_{BV} will become the current density when multiplied by F.

Consider a point (x,y) somewhere on the current collector. The electronic current leaving the current collector and entering the electrode material (or vice versa) is, by definition $J(x,y)$. Consider a piece of the surface around (x,y) with the length ΔL and width ΔW. Both dimensions are assumed to be small, such that $J(x,y)$ does not change much along these dimensions. The electronic current entering the cathode material from the current collector is completely used to form Li^+, generated by the charge transfer reaction on the walls of the pores in the electrode. Therefore, according to the charge conservation law

$$J(x,y)\,\Delta L\,\Delta W = F\int_{A_{tot}^{pores}} j_{BV}(x',y',z')dA, \tag{A20}$$

where A_{tot}^{pores} is the total surface area [m^2] of the active material. The integration in the right-hand side of Eq. (A20) is performed with respect to all pores' surfaces within the cuboid having the basement with the length ΔL, width ΔW, and height δ. The height dimension is orthogonal to the current collector and directed from the surface of this current collector towards the separator. δ is also the thickness of the electrode [m]. Note that

$$A_{tot}^{pores} = aV_{tot} = a\delta\Delta L\Delta W, \tag{A21}$$

in which a is the surface area per unit of volume (specific interfacial area) for the porous electrode [m^{-1}], V_{tot} is the total volume [m^3]. a can be calculated according to [57]

$$a = \frac{A_{tot}^{pores}}{V_{tot}} = \frac{4\pi r^2 N\varepsilon^{sol}}{\frac{4}{3}\pi r^3 N} = \frac{3\varepsilon^{sol}}{r}, \tag{A22}$$

where r represents the mean particle size[m], N is the number of particles and ε^{sol} is the volume fraction of the active material. Eq. (A20) implies that

$$\int_{A_{tot}^{pores}} j_{BV}(x',y',z')dA = a\int_{V_{tot}} j_{BV}(x',y',z')dV. \tag{A23}$$

However, the sub-integral function $j_{BV}(x',y',z')$ in Eq. (A23) does not change too much as a function of (x',y') because $J(x,y)$ does the same. Then

$$\int_{V_{tot}} j_{BV}(x',y',z')dV = \Delta L\Delta W\int_0^{\delta} j_{BV}(x,y,z')dz'. \tag{A24}$$

According to previous reports $j_{BV}(x,y,z')$ considered as a function of z' is close to constant when the battery has good effective electronic and ionic conductivity [17]. Its value can be denoted as $j_{BV}(x,y)$ so that Eq. (A24) simplifies

$$\Delta L\Delta W\int_0^{\delta} j_{bw}(x,y,z')dz' = \Delta L\Delta W\delta j_{BV}(x,y). \tag{A25}$$

Thus, Eq. (A20) takes a form

$$J(x,y) = Fa\delta j_{BV}(x,y). \tag{A26}$$

Furthermore, combining Eqs. (A19) and (A26) gives

$$\eta = \frac{RT}{Fa\delta j^0}J, \tag{A27}$$

therefore

$$\Delta J = \frac{Fj^0\delta a}{RT}\Delta\eta. \tag{A28}$$

According to Eqs. (A18) and (A28), one can finally obtain

$$\Delta J = -\frac{\rho^* I\{(x,y)\in \mathbf{S}^*\}}{\rho H^* A^*} + \frac{\rho^* J(x,y)}{\rho H^*} - \frac{\rho_* I\{(x,y)\in \mathbf{S}_*\}}{\rho H_* A_*} + \frac{\rho_* J(x,y)}{\rho H_*}, \tag{A29}$$

where $\rho = \frac{RT}{Fa\delta j^0}$.

Eq. (A29) was developed for arbitrary electrode. More rigorously, the anode and the cathode contributions to the total overvoltage should be considered together. Thus

$$\eta = \eta_a + \eta_c, \tag{A30}$$

then

$$\eta = \frac{RT}{Fa_a\delta_a j_a^0}J + \frac{RT}{Fa_c\delta_c j_c^0}J = \frac{RT}{F}\left(\frac{1}{a_a\delta_a j_a^0} + \frac{1}{a_c\delta_c j_c^0}\right)J. \tag{A31}$$

In which the subscript a stands for anode and c represents cathode. Consequently

$$\Delta J = \frac{\rho^* J(x,y)}{\rho_{bat}H^*} + \frac{\rho_* J(x,y)}{\rho_{bat}H_*} - \frac{\rho^* I\{(x,y)\in \mathbf{S}^*\}}{\rho_{bat}H^*A^*} - \frac{\rho_* I\{(x,y)\in \mathbf{S}_*\}}{\rho_{bat}H_*A_*}, \tag{A32}$$

where

$$\rho_{bat} = \frac{RT}{F}\left(\frac{1}{a_a\delta_a j_a^0} + \frac{1}{a_c\delta_c j_c^0}\right). \tag{A33}$$

ρ_{bat} [$\Omega\cdot m^2$] is related to the total Bulter–Volmer resistance.
Denote

$$\widehat{\rho}^* = \frac{\rho^*}{H^*} \tag{A34}$$

$$\widehat{\rho}_* = \frac{\rho_*}{H_*} \tag{A35}$$

Substituting Eqs. (A34) and (A35) into Eq. (A32) to make it more compact and gives the final expression of the current density

$$\Delta J = \frac{\widehat{\rho}^* + \widehat{\rho}_*}{\rho_{bat}}J - \frac{\widehat{\rho}^* I\{(x,y)\in \mathbf{S}^*\}}{\rho_{bat}A^*} - \frac{\widehat{\rho}_* I\{(x,y)\in \mathbf{S}_*\}}{\rho_{bat}A_*}. \tag{A36}$$

References

[1] Y. Tian, G. Zeng, A. Rutt, T. Shi, H. Kim, J. Wang, J. Koettgen, Y. Sun, B. Ouyang, T. Chen, Z. Lun, Z. Rong, K. Persson, G. Ceder, Promises and challenges of next-generation "Beyond Li-ion" batteries for electric vehicles and grid decarbonization, Chem. Rev. 121 (2021) 1623–1669, https://doi.org/10.1021/acs.chemrev.0c00767.

[2] X. Lai, C. Jin, W. Yi, X. Han, X. Feng, Y. Zheng, M. Ouyang, Mechanism, modeling, detection, and prevention of the internal short circuit in lithium-ion batteries: recent advances and perspectives, Energy Storage Mater. 35 (2021) 470–499, https://doi.org/10.1016/j.ensm.2020.11.026.

[3] L. Jian, H. Zechun, D. Banister, Z. Yongqiang, W. Zhongying, The future of energy storage shaped by electric vehicles: a perspective from China, Energy 154 (2018) 249–257, https://doi.org/10.1016/j.energy.2018.04.124.

[4] Y. Lv, G. Liu, G. Zhang, X. Yang, A novel thermal management structure using serpentine phase change material coupled with forced air convection for cylindrical battery modules, J. Power Sources 468 (2020), 228398, https://doi.org/10.1016/j.jpowsour.2020.228398.

[5] T.M.M. Heenan, I. Mombrini, A. Llewellyn, S. Checchia, C. Tan, M.J. Johnson, A. Jnawali, G. Garbarino, R. Jervis, D.J.L. Brett, M. Di Michiel, P.R. Shearing, Mapping internal temperatures during high-rate battery applications, Nature 617 (2023) 507–512, https://doi.org/10.1038/s41586-023-05913-z.

[6] S.V. Erhard, P.J. Osswald, P. Keil, E. Höffer, M. Haug, A. Noel, J. Wilhelm, B. Rieger, K. Schmidt, S. Kosch, F.M. Kindermann, F. Spingler, H. Kloust, T. Thoennessen, A. Rheinfeld, A. Jossen, Simulation and measurement of the current density distribution in lithium-ion batteries by a multi-tab cell approach, J. Electrochem. Soc. 164 (2017) A6324–A6333, https://doi.org/10.1149/2.0551701jes.

[7] G. Zhang, C.E. Shaffer, C.-Y. Wang, C.D. Rahn, Effects of non-uniform current distribution on energy density of Li-ion cells, J. Electrochem. Soc. 160 (2013) A2299, https://doi.org/10.1149/2.061311jes.

[8] J. Vetter, P. Novák, M.R. Wagner, C. Veit, K.-C. Möller, J.O. Besenhard, M. Winter, M. Wohlfahrt-Mehrens, C. Vogler, A. Hammouche, Ageing mechanisms in lithium-ion batteries, J. Power Sources 147 (2005) 269–281, https://doi.org/10.1016/j.jpowsour.2005.01.006.

[9] Z. Nie, P. McCormack, H.Z. Bilheux, J.C. Bilheux, J.P. Robinson, J. Nanda, G. M. Koenig, Probing lithiation and delithiation of thick sintered lithium-ion battery electrodes with neutron imaging, J. Power Sources 419 (2019) 127–136, https://doi.org/10.1016/j.jpowsour.2019.02.075.

[10] H. Murayama, K. Kitada, K. Fukuda, A. Mitsui, K. Ohara, H. Arai, Y. Uchimoto, Z. Ogumi, E. Matsubara, Spectroscopic X-ray diffraction for microfocus inspection of Li-ion batteries, J. Phys. Chem. C 118 (2014) 20750–20755, https://doi.org/10.1021/jp5029273.

[11] F. Brauchle, F. Grimsmann, O. von Kessel, K.P. Birke, Direct measurement of current distribution in lithium-ion cells by magnetic field imaging, J. Power Sources 507 (2021), 230292, https://doi.org/10.1016/j.jpowsour.2021.230292.

[12] G. Zhang, C.E. Shaffer, C.-Y. Wang, C.D. Rahn, In-Situ measurement of current distribution in a Li-ion cell, J. Electrochem. Soc. 160 (2013) A610, https://doi.org/10.1149/2.046304jes.

[13] R. Rizk, H. Louahlia, H. Gualous, P. Schaetzel, G. Alcicek, Experimental analysis on Li-ion battery local heat distribution, J. Therm. Anal. Calorim. 138 (2019) 1557–1571, https://doi.org/10.1007/s10973-019-08283-9.

[14] M.J. Mühlbauer, D. Petz, V. Baran, O. Dolotko, M. Hofmann, R. Kostecki, A. Senyshyn, Inhomogeneous distribution of lithium and electrolyte in aged Li-ion cylindrical cells, J. Power Sources 475 (2020), 228690, https://doi.org/10.1016/j.jpowsour.2020.228690.

[15] X.M. Liu, C.B. Arnold, Effects of current density on defect-induced capacity fade through localized plating in lithium-ion batteries, J. Electrochem. Soc. 167 (2020), 130519, https://doi.org/10.1149/1945-7111/abb838.

[16] M.G. Bason, T. Coussens, M. Withers, C. Abel, G. Kendall, P. Kruger, Non-invasive current density imaging of lithium-ion batteries, Appl. Phys. (2021). http://arxiv.org/abs/2103.03358. (Accessed 11 April 2021).

[17] Z. Chen, D.L. Danilov, R.-A. Eichel, P.H.L. Notten, On the reaction rate distribution in porous electrodes, Electrochem. Commun. 121 (2020), 106865, https://doi.org/10.1016/j.elecom.2020.106865.

[18] Y. Tang, M. Jia, J. Li, Y. Lai, Y. Cheng, Y. Liu, Numerical analysis of distribution and evolution of reaction current density in discharge process of lithium-ion power battery, J. Electrochem. Soc. 161 (2014) E3021, https://doi.org/10.1149/2.004408jes.

[19] J. Sturm, A. Rheinfeld, I. Zilberman, F.B. Spingler, S. Kosch, F. Frie, A. Jossen, Modeling and simulation of inhomogeneities in a 18650 nickel-rich, silicon-graphite lithium-ion cell during fast charging, J. Power Sources 412 (2019) 204–223, https://doi.org/10.1016/j.jpowsour.2018.11.043.

[20] P. Taheri, A. Mansouri, B. Schweitzer, M. Yazdanpour, M. Bahrami, Electrical constriction resistance in current collectors of large-scale lithium-ion batteries, J. Electrochem. Soc. 160 (2013) A1731–A1740, https://doi.org/10.1149/2.041310jes.

[21] S.V. Erhard, P.J. Osswald, J. Wilhelm, A. Rheinfeld, S. Kosch, A. Jossen, Simulation and measurement of local potentials of modified commercial cylindrical cells, J. Electrochem. Soc. 162 (2015) A2707, https://doi.org/10.1149/2.0431514jes.

[22] D.A.H. McCleary, J.P. Meyers, B. Kim, Three-dimensional modeling of electrochemical performance and heat generation of spirally and prismatically wound lithium-ion batteries, J. Electrochem. Soc. 160 (2013) A1931, https://doi.org/10.1149/2.023311jes.

[23] M. Guo, R.E. White, Mathematical model for a spirally-wound lithium-ion cell, J. Power Sources 250 (2014) 220–235, https://doi.org/10.1016/j.jpowsour.2013.11.023.

[24] M. Lu, X. Zhang, J. Ji, X. Xu, Y. Zhang, Research progress on power battery cooling technology for electric vehicles, J. Energy Storage 27 (2020), 101155, https://doi.org/10.1016/j.est.2019.101155.

[25] P.H. Camargos, P.H.J. Dos Santos, I.R. Dos Santos, G.S. Ribeiro, R.E. Caetano, Perspectives on Li-ion battery categories for electric vehicle applications: a review of state of the art, Int. J. Energy Res. 46 (2022) 19258–19268, https://doi.org/10.1002/er.7993.

[26] Z. Huang, C. Zhao, H. Li, W. Peng, Z. Zhang, Q. Wang, Experimental study on thermal runaway and its propagation in the large format lithium ion battery module with two electrical connection modes, Energy 205 (2020), 117906, https://doi.org/10.1016/j.energy.2020.117906.
[27] L. Xu, Y. Lu, C.-Z. Zhao, H. Yuan, G.-L. Zhu, L.-P. Hou, Q. Zhang, J.-Q. Huang, Toward the scale-up of solid-state lithium metal batteries: the gaps between lab-level cells and practical large-format batteries, Adv. Energy Mater. 11 (2021), 2002360, https://doi.org/10.1002/aenm.202002360.
[28] A.A.H. Akinlabi, D. Solyali, Configuration, design, and optimization of air-cooled battery thermal management system for electric vehicles: a review, Renew. Sustain. Energy Rev. 125 (2020), 109815, https://doi.org/10.1016/j.rser.2020.109815.
[29] K.-J. Lee, K. Smith, A. Pesaran, G.-H. Kim, Three dimensional thermal-, electrical-, and electrochemical-coupled model for cylindrical wound large format lithium-ion batteries, J. Power Sources 241 (2013) 20–32, https://doi.org/10.1016/j.jpowsour.2013.03.007.
[30] M.-C. Pang, Y. Wei, H. Wang, M. Marinescu, Y. Yan, G.J. Offer, Large-format bipolar and parallel solid-state lithium-metal cell stacks: a thermally coupled model-based comparative study, J. Electrochem. Soc. 167 (2020), 160555, https://doi.org/10.1149/1945-7111/abd493.
[31] Z. Chen, D.L. Danilov, Q. Zhang, M. Jiang, J. Zhou, R.-A. Eichel, P.H.L. Notten, Modeling NCA/C6-Si battery ageing, Electrochim. Acta 430 (2022), 141077, https://doi.org/10.1016/j.electacta.2022.141077.
[32] V. Laue, F. Röder, U. Krewer, Joint structural and electrochemical modeling: impact of porosity on lithium-ion battery performance, Electrochim. Acta 314 (2019) 20–31, https://doi.org/10.1016/j.electacta.2019.05.005.
[33] Z. Geng, S. Wang, M.J. Lacey, D. Brandell, T. Thiringer, Bridging physics-based and equivalent circuit models for lithium-ion batteries, Electrochim. Acta 372 (2021), 137829, https://doi.org/10.1016/j.electacta.2021.137829.
[34] M. Zhuo, G. Offer, M. Marinescu, Degradation model of high-nickel positive electrodes: effects of loss of active material and cyclable lithium on capacity fade, J. Power Sources. 556 (2023), 232461, https://doi.org/10.1016/j.jpowsour.2022.232461.
[35] L.H.J. Raijmakers, D.L. Danilov, R.-A. Eichel, P.H.L. Notten, An advanced all-solid-state Li-ion battery model, Electrochim. Acta 330 (2020), 135147, https://doi.org/10.1016/j.electacta.2019.135147.
[36] K. Chayambuka, G. Mulder, D.L. Danilov, P.H.L. Notten, Physics-based modeling of sodium-ion batteries part II. Model and validation, Electrochim. Acta 404 (2022), 139764, https://doi.org/10.1016/j.electacta.2021.139764.
[37] N. Kazemi, D.L. Danilov, L. Haverkate, N.J. Dudney, S. Unnikrishnan, P.H. L. Notten, Modeling of all-solid-state thin-film Li-ion batteries: accuracy improvement, Solid State Ion 334 (2019) 111–116, https://doi.org/10.1016/j.ssi.2019.02.003.
[38] D. Danilov, R.a.H. Niessen, P.H.L. Notten, Modeling all-solid-state Li-ion batteries, J. Electrochem. Soc. 158 (2010) A215, https://doi.org/10.1149/1.3521414.
[39] P. Kehne, C. Guhl, Q. Ma, F. Tietz, L. Alff, R. Hausbrand, P. Komissinskiy, Sc-substituted Nasicon solid electrolyte for an all-solid-state Na_xCoO_2/Nasicon/Na sodium model battery with stable electrochemical performance, J. Power Sources 409 (2019) 86–93, https://doi.org/10.1016/j.jpowsour.2018.10.089.
[40] Y. Xie, W. Li, Y. Yang, F. Feng, A novel resistance-based thermal model for lithium-ion batteries, Int. J. Energy Res. 42 (2018) 4481–4498, https://doi.org/10.1002/er.4193.
[41] U.S. Kim, C.B. Shin, C.-S. Kim, Effect of electrode configuration on the thermal behavior of a lithium-polymer battery, J. Power Sources 180 (2008) 909–916, https://doi.org/10.1016/j.jpowsour.2007.09.054.
[42] W. Mei, Q. Duan, C. Zhao, W. Lu, J. Sun, Q. Wang, Three-dimensional layered electrochemical-thermal model for a lithium-ion pouch cell Part II. The effect of units number on the performance under adiabatic condition during the discharge, Int. J. Heat Mass Transf. 148 (2020), 119082, https://doi.org/10.1016/j.ijheatmasstransfer.2019.119082.
[43] S.-H. Ng, F.L. Mantia, P. Novák, A multiple working electrode for electrochemical cells: a tool for current density distribution studies, Angew. Chem. Int. Ed. 48 (2009) 528–532, https://doi.org/10.1002/anie.200803981.
[44] Z. Wang, D.L. Danilov, R.-A. Eichel, P.H.L. Notten, Modeling the resistance of thin-film current collectors in thin-film batteries, J. Electrochem. Soc. 170 (2023) 020514, https://doi.org/10.1149/1945-7111/acb855.
[45] Y. Liu, C. Dong, Y. Qi, Effect of thickness on the surface and electronic properties of Bi Film, Acta Met. Sin. 54 (2018) 935–942, https://doi.org/10.11900/0412.1961.2017.00422.
[46] P. Zhu, D. Gastol, J. Marshall, R. Sommerville, V. Goodship, E. Kendrick, A review of current collectors for lithium-ion batteries, J. Power Sources 485 (2021), 229321, https://doi.org/10.1016/j.jpowsour.2020.229321.
[47] B.-J. Kim, W.-K. Choi, M.-K. Um, S.-J. Park, Effects of nickel coating thickness on electric properties of nickel/carbon hybrid fibers, Surf. Coat. Technol. 205 (2011) 3416–3421, https://doi.org/10.1016/j.surfcoat.2010.12.007.
[48] C. Li, H. Zhang, R. Zhang, Y. Lin, H. Fang, On the characteristics analysis and tab design of an 18650 type cylindrical $LiFePO_4$ battery, Appl. Therm. Eng. 182 (2021), 116144, https://doi.org/10.1016/j.applthermaleng.2020.116144.
[49] S. Du, M. Jia, Y. Cheng, Y. Tang, H. Zhang, L. Ai, K. Zhang, Y. Lai, Study on the thermal behaviors of power lithium iron phosphate (LFP) aluminum-laminated battery with different tab configurations, Int. J. Therm. Sci. 89 (2015) 327–336, https://doi.org/10.1016/j.ijthermalsci.2014.11.018.
[50] X.-Y. Yao, M.G. Pecht, Tab design and failures in cylindrical Li-ion batteries, IEEE Access 7 (2019) 24082–24095, https://doi.org/10.1109/ACCESS.2019.2899793.
[51] S. Li, N. Kirkaldy, C. Zhang, K. Gopalakrishnan, T. Amietszajew, L.B. Diaz, J. V. Barreras, M. Shams, X. Hua, Y. Patel, G.J. Offer, M. Marinescu, Optimal cell tab design and cooling strategy for cylindrical lithium-ion batteries, J. Power Sources 492 (2021), 229594, https://doi.org/10.1016/j.jpowsour.2021.229594.
[52] F. Wang, B. Wang, J. Li, B. Wang, Y. Zhou, D. Wang, H. Liu, S. Dou, Prelithiation: a crucial strategy for boosting the practical application of next-generation lithium ion battery, ACS Nano 15 (2021) 2197–2218, https://doi.org/10.1021/acsnano.0c10664.
[53] P.N. Didwal, Y.N. Singhbabu, R. Verma, B.-J. Sung, G.-H. Lee, J.-S. Lee, D. R. Chang, C.-J. Park, An advanced solid polymer electrolyte composed of poly (propylene carbonate) and mesoporous silica nanoparticles for use in all-solid-state lithium-ion batteries, Energy Storage Mater. 37 (2021) 476–490, https://doi.org/10.1016/j.ensm.2021.02.034.
[54] Q. Xia, Q. Zhang, S. Sun, F. Hussain, C. Zhang, X. Zhu, F. Meng, K. Liu, H. Geng, J. Xu, F. Zan, P. Wang, L. Gu, H. Xia, Tunnel intergrowth LixMnO2 nanosheet arrays as 3D cathode for high-performance all-solid-state thin film lithium microbatteries, Adv. Mater. 33 (2021), 2003524, https://doi.org/10.1002/adma.202003524.
[55] E. Parma, G.F. Costa, R. Nagao, Modeling Li-ion battery voltage oscillations and the impact of exchange current density on oscillation properties, J. Phys. Chem. C 126 (2022) 11900–11906, https://doi.org/10.1021/acs.jpcc.2c03061.
[56] M. Wang, J. Li, X. He, H. Wu, C. Wan, The effect of local current density on electrode design for lithium-ion batteries, J. Power Sources 207 (2012) 127–133, https://doi.org/10.1016/j.jpowsour.2011.12.063.
[57] S. Kosch, Y. Zhao, J. Sturm, J. Schuster, G. Mulder, E. Ayerbe, A. Jossen, A computationally efficient multi-scale model for lithium-ion cells, J. Electrochem. Soc. 165 (2018) A2374, https://doi.org/10.1149/2.1241810jes.